Fractographic Features of Technically Pure Magnesium, AZ31 and ZK60 Alloys Subjected to Stress Corrosion Cracking

Evgeniy Merson[1*], Vitaliy Poluyanov[1], Pavel Myagkikh[1], Dmitri Merson[1], Alexei Vinogradov[2]

[1]*Institute of Advanced Technologies, Togliatti State University, Belorusskaya str. 14, Togliatti 445667, Russian Federation*

[2]*Department of Mechanical and Industrial Engineering, Norwegian University of Science and Technology – NTNU, N-7491 Trondheim, Norway*

**Email: mersoned@gmail.com*

Abstract

Using quantitative fractography, the present study clarifies the effect of chemical composition and preliminary plastic deformation on the fracture mode of structural magnesium alloys experienced stress corrosion cracking (SCC). It is demonstrated that the fracture surfaces of alloys ZK60 and AZ31 failed during slow strain rate testing (SSRT) under SCC conditions are commonly featured by (i) the close-to-side surface region of typically brittle fracture initiation composing of intergranular and cleavage facets, which gradually transforms to (ii) the region of transgranular fluted facets optionally followed by the regions of (iii) fluted facets with secondary cracks, (iv) flat dimpled rapture and (v) slant dimpled rapture. Counterintuitively, the preliminary plastic strain introduced in air results in the increase of the fraction of the ductile mode on the fracture surface, elongation and stress at fracture of both alloys SSRT tested in corrosive media. The positive effect of pre-straining can be likely explained from the mechanistic viewpoint due to the increase of the yield stress, which has to be overcome to trigger plastic deformation needed to break the surface protective film. Features of the SCC mechanisms affecting the fracture surface appearance are quantified and discussed.

Keywords: magnesium alloys; stress corrosion cracking; fractography; plastic deformation

1. Introduction.

Wrought magnesium alloys are considered highly promising low-weight structural metallic materials due to their unique properties profile and versatile application possibilities. Nevertheless, high susceptibility of these materials to corrosion and stress corrosion cracking (SCC) restricts their industrial application. Success in the improvement of SCC resistance of magnesium alloys largely depends on the understanding of the nature of this phenomenon, which is not fully achieved at the day. The SCC of magnesium alloys is usually associated with anodic dissolution (AD) and hydrogen embrittlement (HE). It is suggested that the former can be solely responsible for the intergranular (IG) SCC for example when it occurs due to accelerated dissolution of metal matrix along grain boundaries enriched by β-phase particles nobler with respect to Mg [1]. Alternatively the role of AD can be limited to producing pits which then serve as preferable cites for hydrogen-assisted cracking [2–4]. However, AD cannot produce completely crystallographic and fluted transgranular facets which are frequently found on the fracture surfaces of Mg alloys failed due to transgranular (TG) SCC [2,5–8]. Such observations have prompted some scientists to suggest that SCC in Mg can be caused by HE. It is believed that hydrogen evolving during AD of the base metal can be absorbed by the Mg matrix, thus promoting hydrogen assisted cracking [6]. Despite quite many studies on the issue the exact role of hydrogen in the SCC of Mg alloys was not fully understood.

Chakrapani and Pugh in their pioneering studies, [7,9] established that SCC of the Mg-7.5Al alloy in the aqueous NaC1-K_2CrO_4 solution occurs by transgranular cleavage along the $\{31\bar{4}0\}$ crystallographic planes, which were believed to correspond to the habit or cleavage planes of the Mg hydride. It was supposed that the SCC mechanism involves repeated cycles of hydrogen diffusion to the region ahead of the crack tip followed by cleavage through the hydrogen-enriched zone, admittedly, transformed into hydride [10]. Afterwards, this mechanism referred to as delayed hydride cracking was applied to explain the transgranular cleavage-like fracture surfaces of alloys Mg-Al-Zn, Mg-Al-Mn [2,11] and Mg-Zn-Zr [12] subjected to SCC. The featureless cleavage-like facets with interlocking river patterns exhibiting neither dimples nor other features of ductile fracture are sometimes alternatively explained by the hydrogen-enhanced decohesion (HEDE) mechanism [2,12,13]. The latter mechanism implies that hydrogen atoms, which are segregated in a crystal lattice or at a grain boundary, reduce the cohesive force between metallic atoms belonging to an individual grain or two different crystallites, respectively [14,15]. The weakening of interatomic bonds facilitates the inter- or trans-granular brittle

fracture at the stress lower than it would be in the hydrogen-free metal. Lynch and Trevena [8] found that pure Mg specimens subjected to either liquid metal embrittlement (LME) or SCC exhibited substantially same transgranular fracture surfaces with the characteristic fluted morphology. Since the adsorption is the key mechanism of interaction of liquid metal atoms with a solid metal, the authors supposed that SCC, as well as LME, of Mg is induced by the adsorption of a surface-active agent, which, in the case of SCC, was believed to be hydrogen. According to the adsorption-induced dislocation emission (AIDE) theory [8,15,16], hydrogen adsorbing on a metal surface at a crack tip weakens interatomic bonds, and, thus, facilitates dislocation emission from the crack tip. Stimulated by hydrogen-enhanced dislocation emission, the crack propagates in a ductile manner with nano-void formation eventually producing a fluted relief and seemingly flat cleavage-like facets, which surface is, in fact, composed of shallow nano-sized dimples [8]. The presence of dimples on the surface of the facet was also considered as a factor supporting the hydrogen-enhanced localized plasticity (HELP) theory, c.f. [2] and [12] for the alloys AZ31, AZ91 and ZK60, respectively. According to this theory, which has been proposed first for iron and steels [17], atomic hydrogen, segregating at dislocations, screens their elastic fields and decreases the Peierls barrier, thus giving rise to the increase in the density and mobility of dislocations. When the external stress is applied, diffusible hydrogen concentrates at the regions of maximum triaxial stresses ahead of the crack tip, stimulating the locally enhanced ductile fracture.

As follows from the brief literature survey, SCC of Mg and its alloys can produce the typically brittle intergranular and transgranular cleavage facets as well as transgranular facets featuring by dimples and flutes. However, the role of hydrogen and the factors controlling the SCC fracture mode in Mg-based alloys have not been understood as yet. The present study aims at clarifying the effect of chemical composition and preliminary deformation on the fracture mode of Mg alloys subjected to SCC. The quantitative fractographic analysis is employed to attain this goal.

2. Experimental

In the present investigation, we focus on the in-depth fractographic analysis of the specimens which have been subjected to slow strain rate tensile (SSRT) testing in air or in corrosive media as has been described in detail in our companion paper reporting the results of the gas analysis in the same specimens [18]. The brief description of conducted experiments is given below.

The round, threaded 120 mm long specimens with the 6 mm diameter and 30 mm long gauge part were machined from the ingot of as-cast technically pure magnesium as well as from the commercially available hot rolled sheet of the alloy AZ31 (MA2-1 in Russian designation) and the extruded round bar of the alloy ZK60 (MA14). Chemical compositions of the materials are provided in Table 1. The average grain size was of 3 mm, 10 and 3 μm for pure Mg, and alloys AZ31 and ZK60, respectively. The SSRT testing of the initial (as-received) specimens was conducted using the Instron type screw-driven frame at the nominal strain rate of $5 \cdot 10^{-6}$ s^{-1} in air and in corrosive media (the aqueous 5g/l NaCl + 5g/l $K_2Cr_2O_7$ solution). To evaluate the effect of pre-straining on SCC, several ZK60, AZ31 and pure Mg specimens were plastically deformed in air to 4, 11 and 2% tensile strain, respectively. After unloading, the pre-strained specimens were SSRT tested in corrosive media in the same way as their as-received counterparts.

The fractographic analysis of the broken specimens was performed using the field-emission scanning electron microscope (SEM) SIGMA, Zeiss.

Table 1 – Chemical composition of the alloys (in wt. %)

Material	**Mg**	**Al**	**Zn**	**Ca**	**Zr**	**Fe**	**Cu**	**Mn**	**Ce**	**Nd**	**Si**
ZK60		0.002	5.417	0.0004	0.471	0.001	0.002	0.005	0.002	0.003	0.003
AZ31	Balance	4.473	0.887	0.0015	-	0.002	0.003	0.312	0.017	0.007	0.008
Pure Mg		0.005	-	0.0002	-	0.067	-	0.002	0.009	0.001	0.003

3. Results

The results of mechanical testing, metallographic observations of the microstructure and the gas-analysis were documented in detail in [18]. Here, for the sake of self-consistency, we present only a brief survey of the most relevant results.

3.1. As-cast pure Mg

Non-surprisingly, as-cast pure Mg exhibits very poor mechanical properties, Table 2. The elongation to failure in air does not exceed 7%, while the yield stress and the ultimate tensile strength are as low as 15 and 55 MPa, respectively. The fracture of the specimens tested in air occurs after pronounced strain-hardening without the significant necking stage. The specimens tested in corrosive media demonstrate lower elongation to failure, yield and ultimate tensile

stresses than in air. Interestingly is that strain-hardening of Mg specimens in corrosive media occurs at the lower stress than in air, i.e. softening occurs. The pre-straining results in the increase of the yield stress of the specimens tested in corrosive media while the ductility, which is assessed by their elongation to failure, is compromised in comparison with that in the as-received counterparts.

After testing in air, the fracture surface of the as-cast Mg specimens consists predominantly of transgranular fluted facets, Fig. 1a, b, similar to those found in [8]. As is illustrated by Fig.1d, f, the fluted morphology of pure Mg tested in air exhibits many dimples within the flutes. Besides the fluted ones, a few facets demonstrating smoother appearance were found on the fracture surface of these specimens, c.f. Fig. 1c, e.

The fracture surface of the as-cast Mg specimens tested in corrosive media also exhibits the characteristic fluted relief, Fig. 2. Nevertheless, the flutes do not contain either dimples or transverse tear ridges, so that the surface of the flutes looks much smoother than that after testing in air as can be seen in Fig. 2d, f. The number of smooth facets, such as those shown in Fig. 2c, e, is somehow larger in the SCC-tested Mg specimens in comparison with the specimens tested in air, though, taking into account the large grain size of the material, the statistical nature of this observation cannot be excluded.

The pre-strained specimens of pure Mg tested in corrosive media also demonstrate fluted facets on the fracture surface. No significant qualitative or quantitative fractographic differences are found between the ordinary and pre-strained specimens tested in the corrosive solution.

Table 2 – Conventional 0.2% yield stress σ_y, ultimate tensile strength σ_{UTS}, elongation to failure δ and fracture surface features for as-cast technically pure Mg, and AZ31 and ZK60 alloy specimens SSRT-tested at different conditions.

Alloy	Testing conditions	σ_y, MPa	σ_{UTS}, MPa	δ, %	Fracture surface features		
					a_1 (Brittle IG+C), μm	a_2 (Fluted), μm	a_3 (Dimpled), μm
As-cast Mg	In air	15±1	55±6	6.9±0.1	Flutes with dimples + scarce smooth facets		
	In corrosive media	12±1	26±3	5.6±0.3	Flutes + scarce smooth facets		
	In corrosive media after pre-straining	30±8	42±3	3.6±1.2	Flutes + scarce smooth facets		
ZK60	In air	254±8	296±1	28.3±2.1	Dimples		

	In corrosive media	-	157±20	2.2±0.3	531±106	2503±520	3045±278
	In corrosive media after pre-straining	-	224±16	2.9±0.2	367±64	1785±178	3945±43
AZ31	In air	147±3	272±2	25.1±1.2	Dimples		
	In corrosive media	-	129±11	2.6±0.1	1032±328	3679±574	792±332
	In corrosive media after pre-straining	-	145±6	2.7±0.1	878±14	1620±737	3049±492

3.2. Alloy ZK60

Among the investigated materials, the alloy ZK60 possess higher mechanical properties in terms of the elongation to failure, yield stress and ultimate tensile strength in air, Table 2. After SSRT testing in corrosive media, the fracture persistently occurs at stresses around $0.7\sigma_y$. One should notice that the preliminary straining considerably reduces the susceptibility of the specimens to SCC as is indicated by the fracture stress (of $0.9\sigma_y$) which is notably higher than that in the as-received counterparts SSRT tested under the same conditions.

The fracture surface of ZK60 specimens tested in air is completely ductile with the typical dimpled relief illustrated in Fig. 3.

The specimens SSRT tested in corrosive media demonstrate partially brittle fracture surfaces, Fig. 4. In all tested specimens, the brittle fracture initiated at one side of the specimen while the opposite side failed in a ductile manner, Fig. 4a. A few brittle cracks originated at the side surface and propagated towards the central part of the specimen, c.f. Figs. 4b-d. This is indicated by the fan-like macro ridges, which are radiated from several points at the peripheral part of the fracture surface as is indicated by the arrows in Fig. 4a. In all specimens, the path of the largest main central crack, such as that shown in Fig. 4c, can be identified on the fracture surface. As is illustrated by the schematics shown in Fig. 5, five distinct zones following one by one between the two opposite side surfaces can be distinguished along the crack path on the fracture surface. The first zone begins at the side surface and spreads towards the specimen centre up to the distance a_1 = 450-600 μm, c.f. Table 2. The corrosion products (indicated by arrows in Fig. 6a) are found on the fracture surface in the region close to the specimen's side surface. The morphology of the first zone is represented by the mixture of typically brittle

intergranular and cleavage facets as shown in Figs. 6b-f. These facets are featured by the interlocking step-like river lines patterns, which are clearly seen in Figs. 6c and e. Most of the intergranular facets, e.g. Figs. 6b, d, f, exhibit clear signatures of anodic dissolution. Along the crack path, the morphology of the zone a_1 gradually transforms into the next zone, a_2, featured by smooth fluted transgranular facets, Fig. 7. The smooth morphology of the flutes, Figs. 7c-f, is rather similar to that in as-cast pure Mg tested in corrosive media, Fig. 2f, than to the dimpled ones produced during fracture in air, Fig. 1f. Although the flutes in the fractured alloy ZK60 are somewhat less pronounced than in pure Mg, they are still undoubtedly distinguishable. The mixed cleavage and fluted facets corresponding to the same grain can be occasionally found in the transition region between the first and the second zones, Fig. 7b. Such facets demonstrate the flutes oriented perpendicular to the neighbouring river lines, Fig. 7d. It is known that the river lines of the cleavage facets orient along the crack growth direction. As such, the flutes are aligned transverse to the crack growth direction.

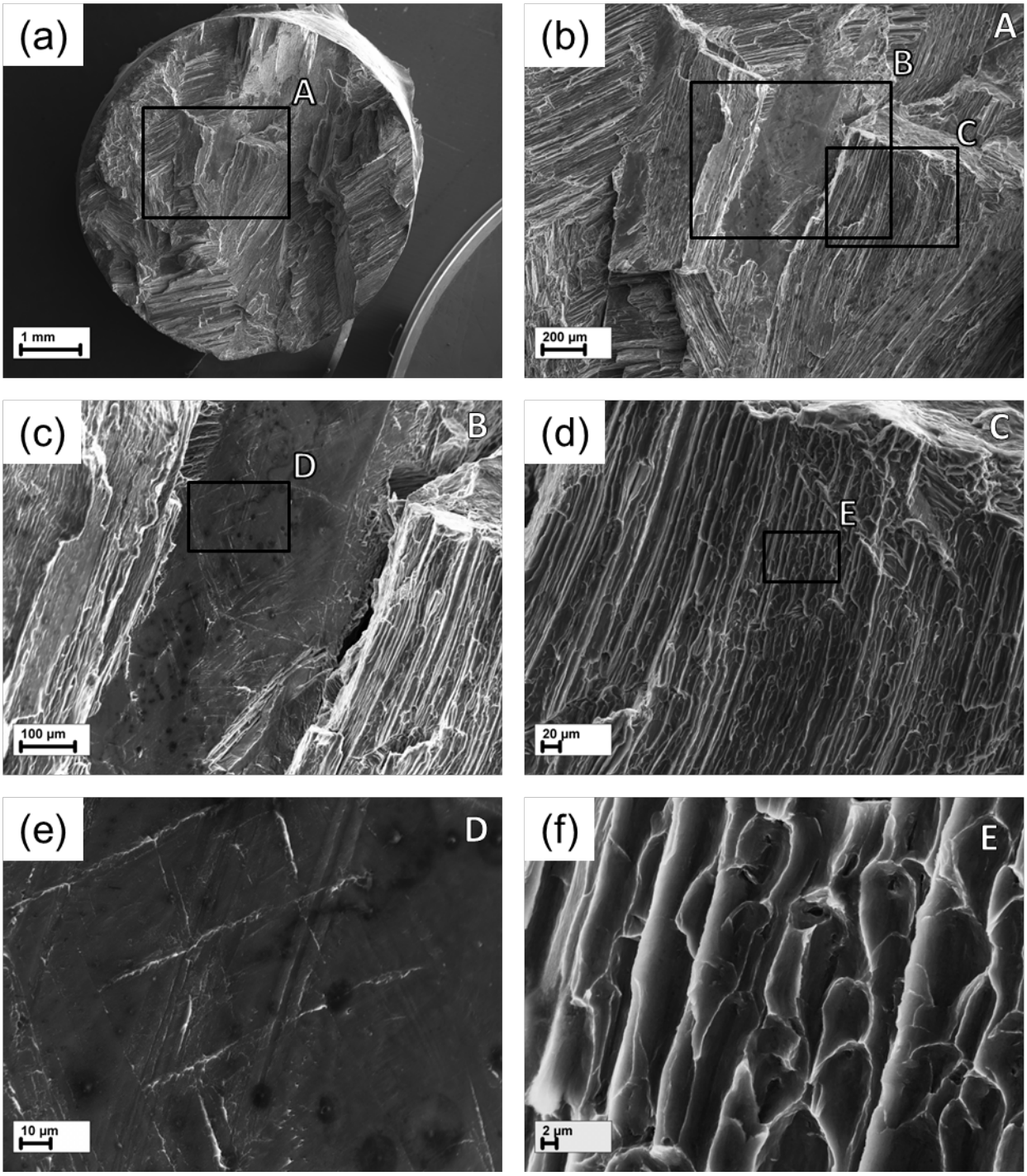

Fig. 1 – Fractographic SEM images of the as-cast pure Mg specimens tested in air: (a) – full view; (b) – the magnified region marked as A in (a) containing fluted and smooth facets; (c) – magnified region marked as B in (b) demonstrating smooth brittle facet; (d) – magnified region marked as C in (b) showing the fluted facet; (e) – magnified region marked as D in (c) demonstrating traces of different slip systems on the surface of the smooth facet; (f) – magnified region marked as E in (d) demonstrating dimples within the flutes of the fluted facet.

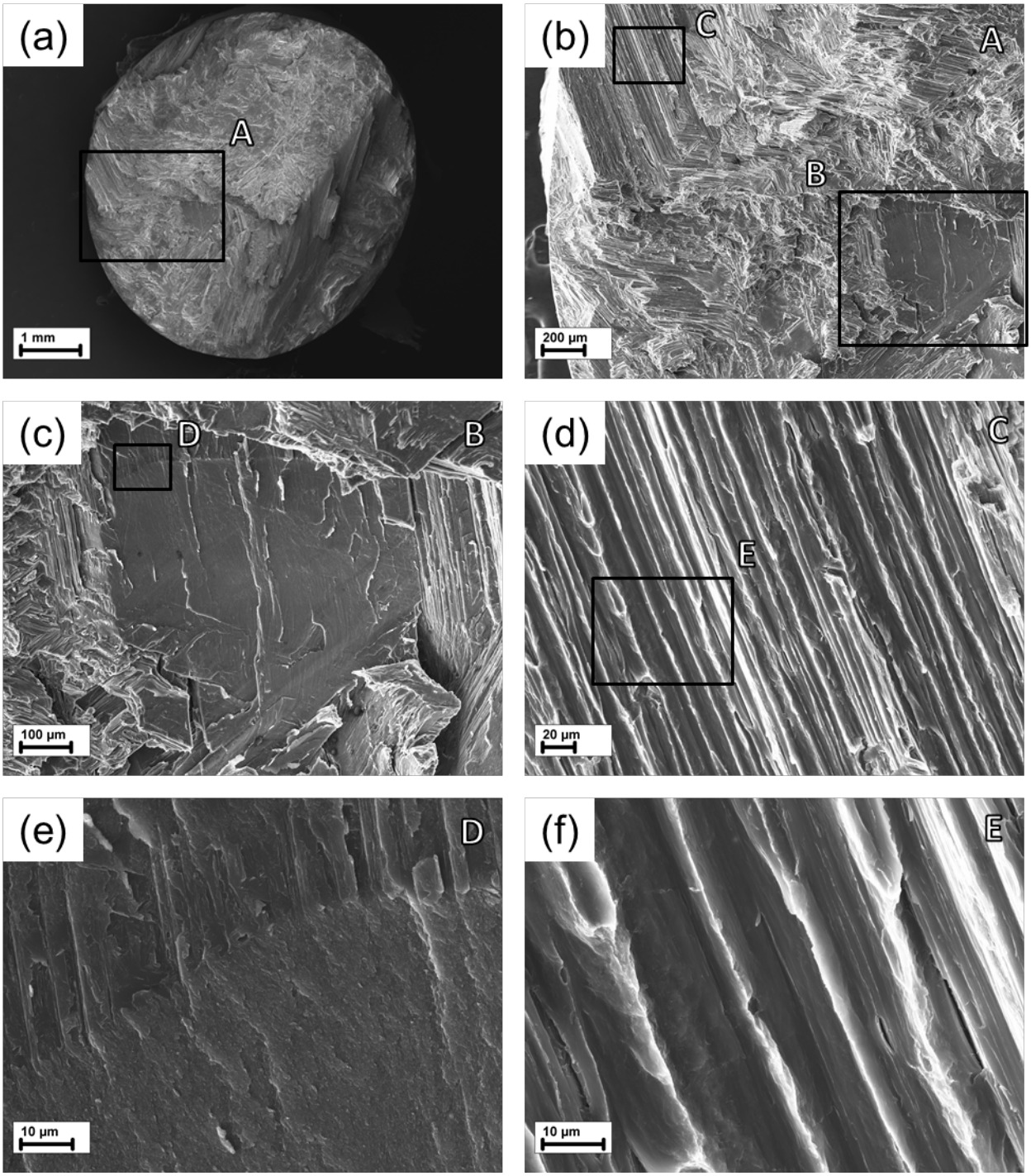

Fig. 2 – Fractographic SEM images of the as-cast pure Mg specimens tested in corrosive media: (a) – full view; (b) – the magnified region marked as A in (a) containing fluted and smooth facets; (c) – magnified region marked as B in (b) demonstrating smooth brittle facet; (d) – magnified region marked as C in (b) showing the fluted facet; (e) – magnified region marked as D in (c) demonstrating morphology of the smooth facet; (f) – magnified region marked as E in (d) demonstrating smooth surface of the flutes.

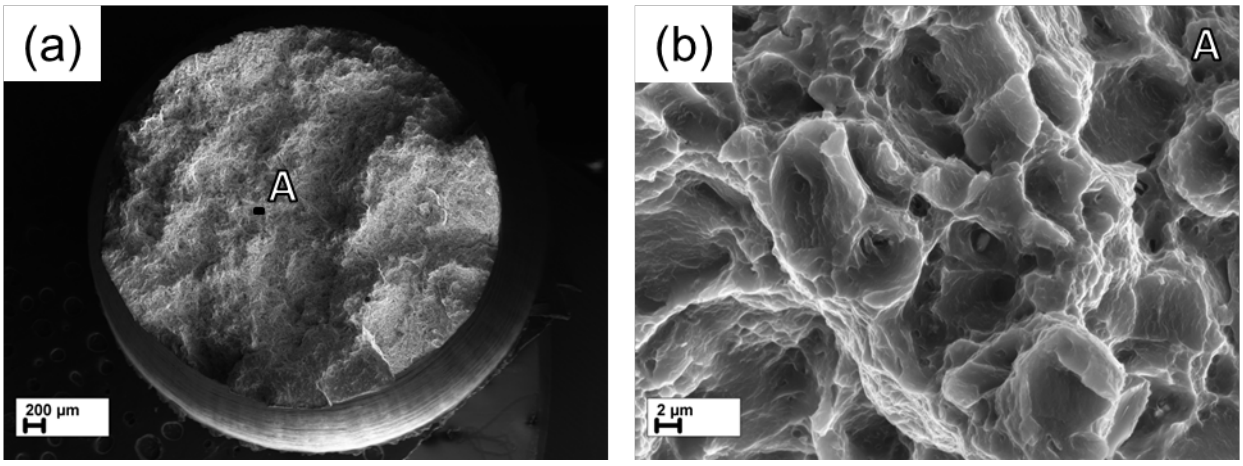

Fig. 3 – Fractographic SEM images of the ZK60 specimens tested in air: (a) – full view; (b) – the magnified region marked as A in (a) demonstrating typical ductile dimpled relief.

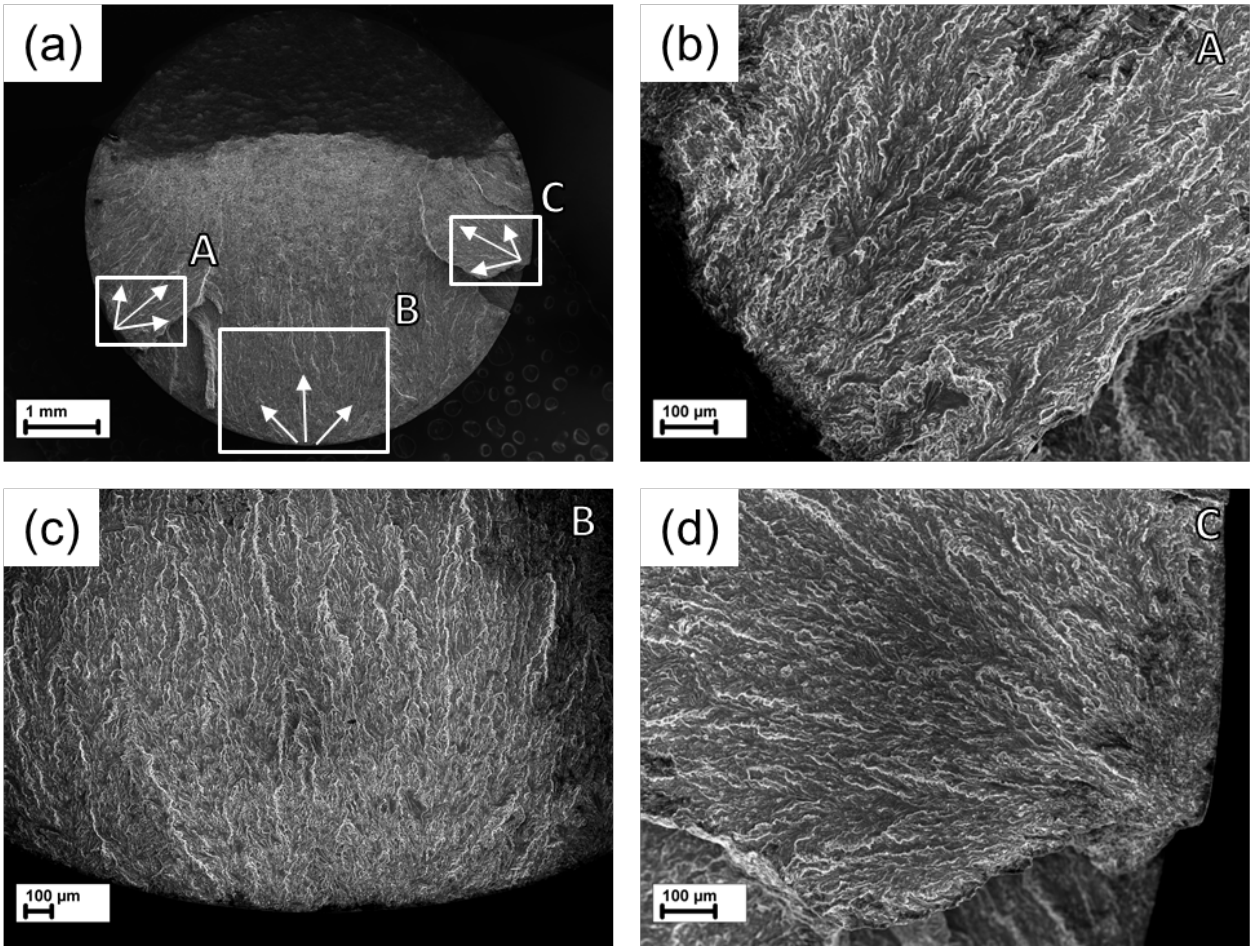

Fig. 4 – Fractographic SEM images of the ZK60 specimens tested in corrosive media: (a) – full view; (b) – the magnified region marked as A in (a); (c) – the magnified region marked as B in (a); (d) – the magnified region marked as C in (a).

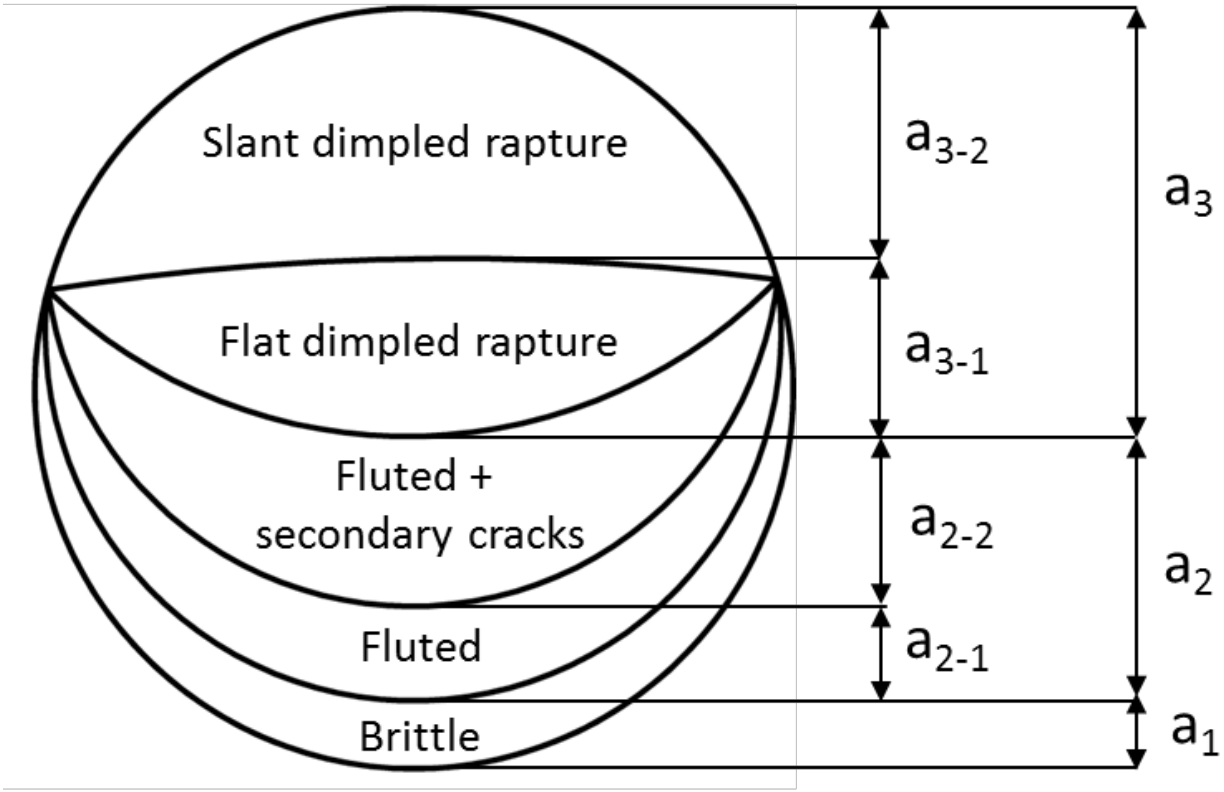

Fig. 5 – Schematic representation of the morphologically different zones on the fracture surface of the ZK60 specimens tested in corrosive media.

In order to evaluate the characteristic length scales of the morphologically different zones distinguished on the fracture surface, the boundary between the first and the second zones was contingently defined according to the first appearance of the fluted facets. It was established that the area of the fracture surface covered by the fluted facets extends up to the distance a_2 ranging between 2100 and 2900 μm, Table 2. In this area, the fluted morphology evidently prevails, Fig. 8. One can notice that approximately in the middle part of the zone 2, the secondary cracks appear and are systematically observed until the end of this zone, Fig. 9. The part of the a_2 zone, which is free of the secondary cracks, and the one containing the secondary cracks were defined as the subzones 2-1 and 2-2, respectively. Their corresponding length scales $a_{2\text{-}1}$ and $a_{2\text{-}2}$ are found to be varied in the ranges of 1200-1400 μm and 900-1500 μm, respectively. As is illustrated by Fig. 9b, the secondary cracks can grow along the flutes as well as across them. At higher magnification, it can be seen that the growth of the secondary cracks was accompanied by the formation and coalescence of microvoids having 0.5-2 μm diameters, c.f. Figs. 9c-f.

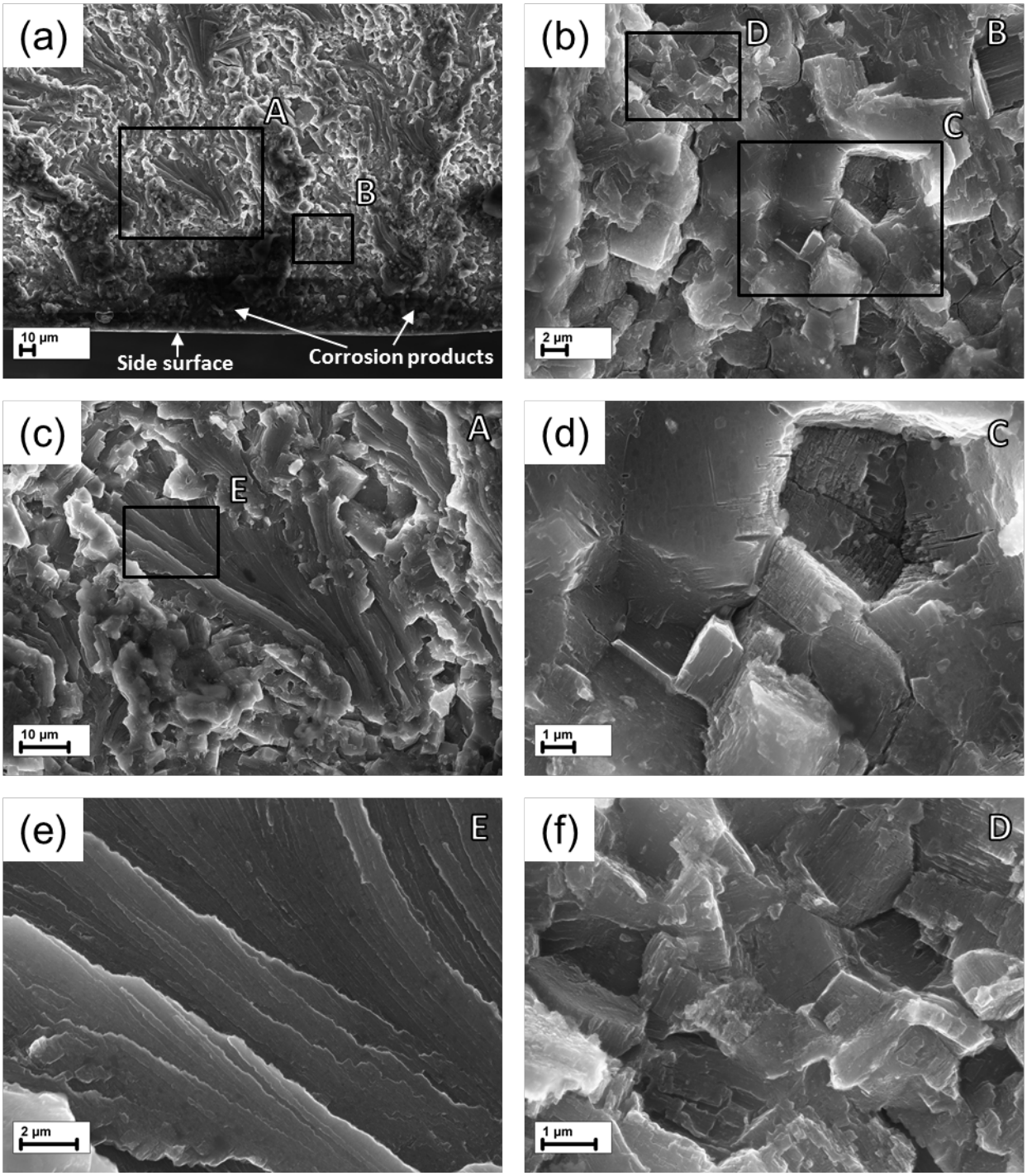

Fig. 6 – Fractographic SEM images of the zone a_1 featuring by brittle intergranular and cleavage facets for the ZK60 specimens tested in corrosive media: (a) – general view; (b) – the magnified region marked as B in (a) containing intergranular facets; (c) – the magnified region marked as A in (a) demonstrating transgranular cleavage facet; (d) – the magnified region marked as C in (b) showing the intergranular facets; (e) – the magnified region marked as E in (c) demonstrating interlocking river pattern of the cleavage facet; (f) – the magnified region marked as D in (b) demonstrating fine intergranular facets.

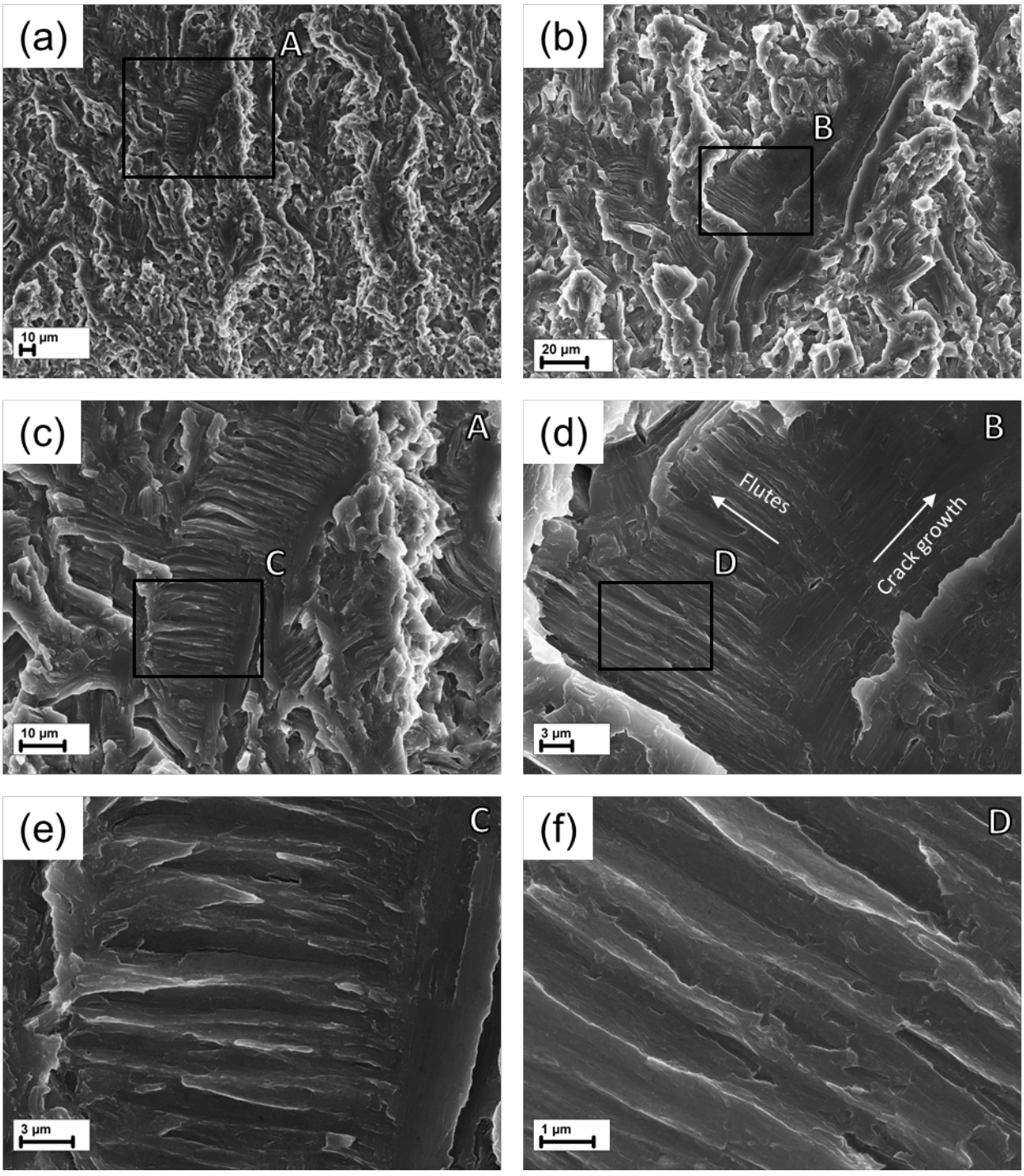

Fig. 7 – Fractographic SEM images of the transition region between the zones a_1 and a_2 for the alloy ZK60 specimens tested in corrosive media: (a) – the region with the first fluted facet of the zone a_2; (b) – the region with the transgranular facet of the mixed cleavage/fluted type; (c) – the magnified region marked as A in (a) demonstrating the fluted facet; (d) – the magnified region marked as B in (b) showing the flutes and river lines within the same facet; (e) – the magnified region marked as C in (c) demonstrating flutes; (f) – magnified region marked as D in (d) demonstrating flutes.

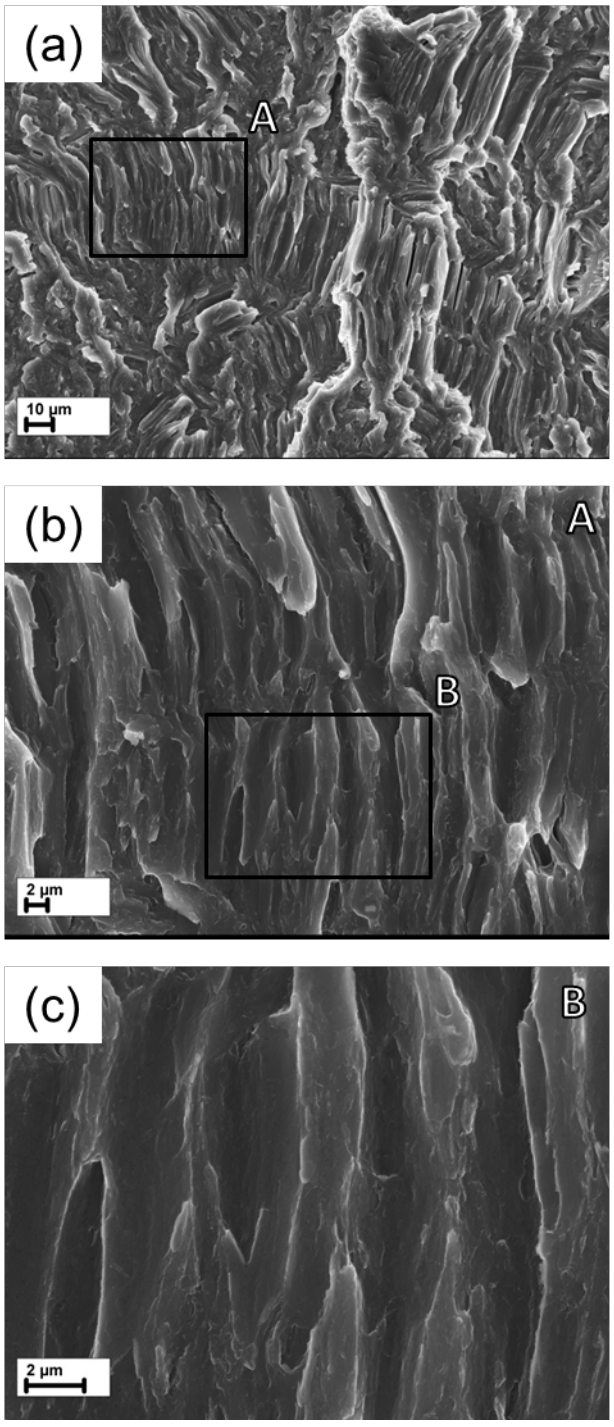

Fig. 8 – Fractographic SEM images of the zone $a_{2\text{-}1}$ featuring by fluted facets for the alloy ZK60 specimens tested in corrosive media: (a) – the region with the prevailing fluted morphology; (b) – the magnified region marked as A in (a); (c) – the magnified region marked as B in (b);

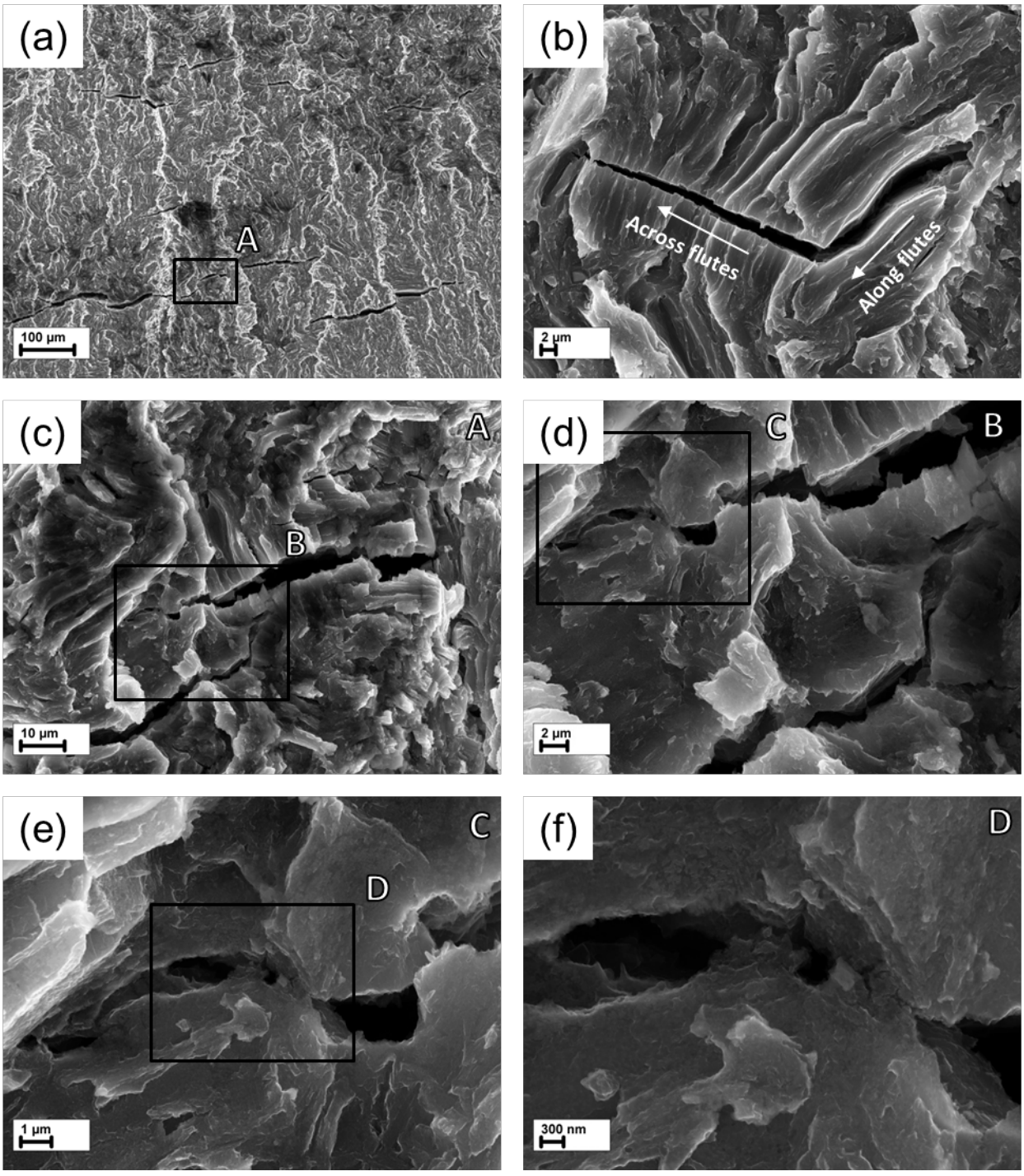

Fig. 9 – Fractographic SEM images of the zone $a_{2\text{-}2}$ featuring by the fluted morphology and secondary cracks for the alloy ZK60 specimens tested in corrosive media: (a) – general view; (b) – the secondary crack growing along and across the flutes; (c) – the magnified region marked as A in (a) demonstrating secondary cracks; (d) – the magnified region marked as B in (c); (e) – the magnified region marked as C in (d) demonstrating coalescing voids at the crack tip; (f) – magnified region marked as D in (e).

At the end of the zone a_2, the fluted morphology gradually transforms into the ductile dimpled relief typical of the third zone. In the transition region between the second and the third zones, both flutes and dimples can be observed interchangeably, c.f. Figs. 10a, b. Beyond the transition region, the morphology of the third zone demonstrates the completely ductile dimpled relief, Fig. 11. Its length a_3 is ranged approximately from 2850 to 3250 μm for different specimens. The first part of the third zone close to the fluted area is oriented normally to the specimen tensile axis and has the length $a_{3\text{-}1}$ = 1600-1750 μm. Next to this region, the fracture surface is inclined at ≈45º to the tensile axis. The length of this region is $a_{3\text{-}2}$ = 1250-1500 μm. Typical dimpled morphologies of the subzones 3-1 and 3-2 are represented in Figs. 11a, b and c, d, respectively.

Qualitatively, the fracture surfaces of the pre-strained specimens failed due to SCC demonstrate the same topological features and distinct zones as the as-received specimens. However, the area of the ductile zone 3 is notably larger while the characteristic lengths of the zones a_1 and a_2 produced due to SCC are admittedly smaller in the pre-strained specimens, Table 2. This observation is in agreement with the higher mechanical properties of the pre-strained specimens.

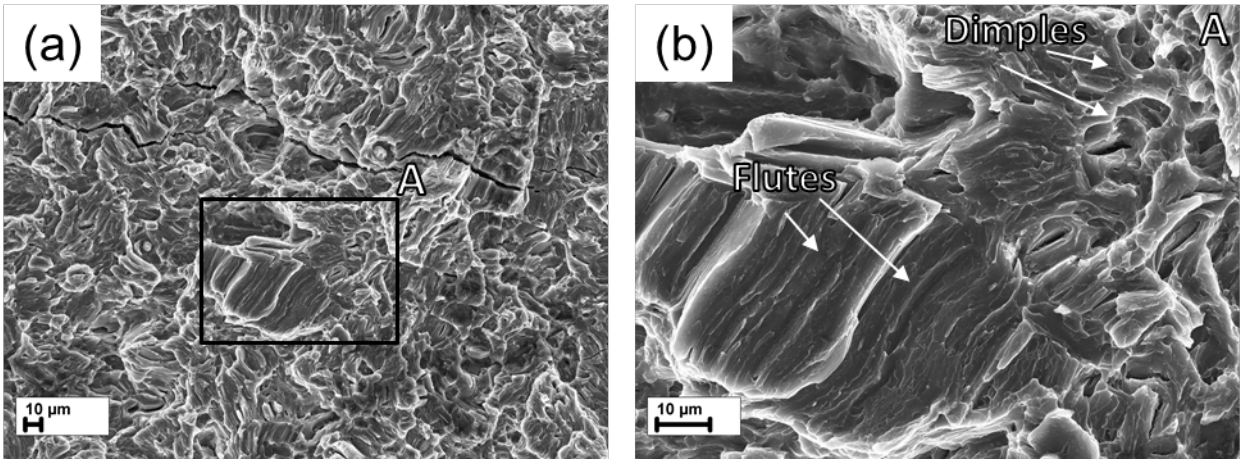

Fig. 10 – Fractographic SEM images of the transition region between the zones a_2 and a_3 for the ZK60 specimens tested in corrosive media: (a) – general view; (b) – the magnified region marked as A in (a) demonstrating fluted facets neighboring the dimples.

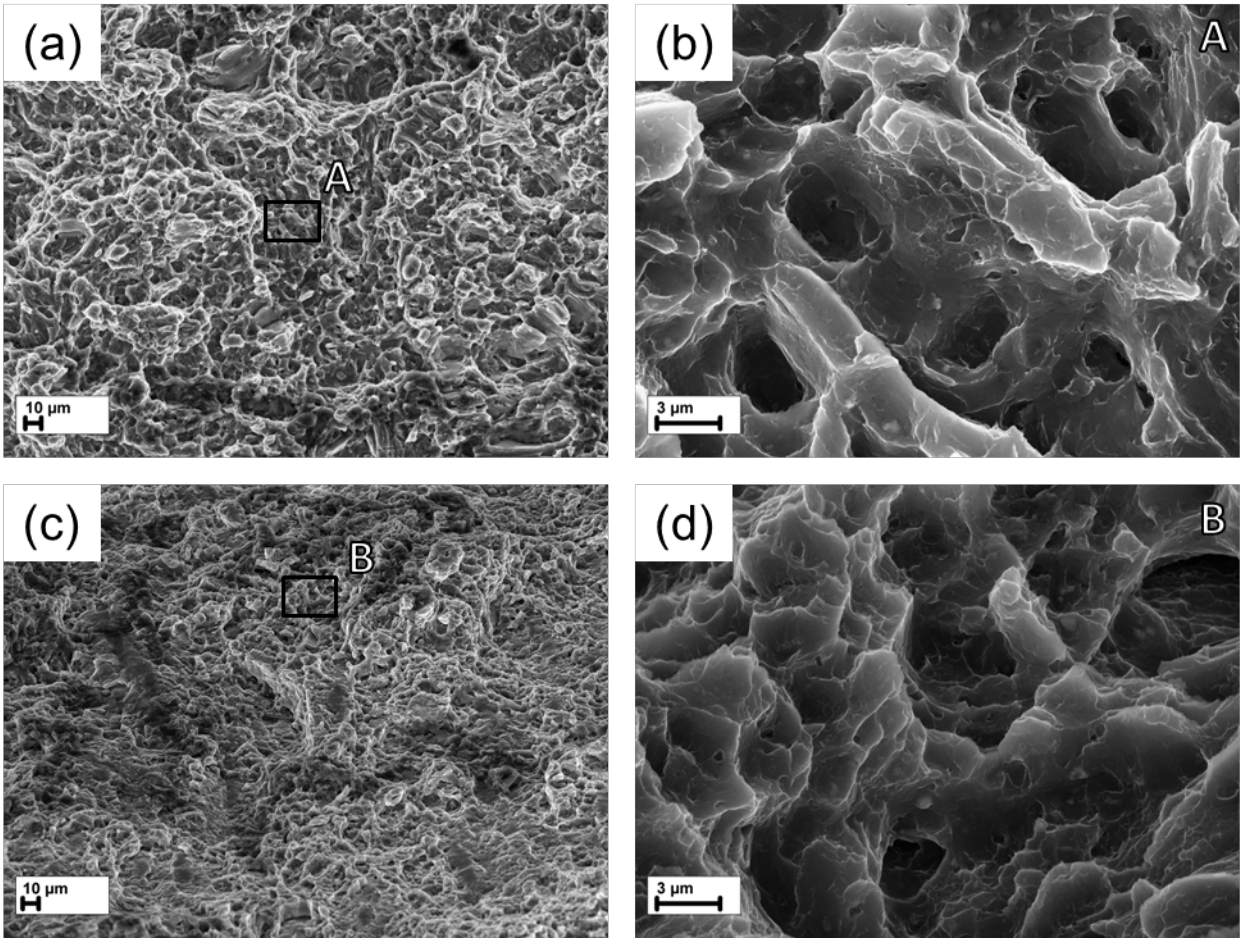

Fig. 11 – Fractographic SEM images of the zone 3 featuring by dimpled relief for the ZK60 specimens tested in corrosive media: (a) – general view of the zone $a_{3\text{-}1}$; (b) – the magnified region marked as A in (a) demonstrating dimpled relief; (b) – general view of the zone $a_{3\text{-}2}$; (d) – the magnified region marked as B in (c) demonstrating dimpled relief.

3.3. Alloy AZ31

The elongation to failure and the ultimate tensile strength of the alloy AZ31 tested in air are close to those of the alloy ZK60, whereas its yield stress is almost twice lower. The tensile tested AZ31 specimens exhibit the pronounced strain-hardening region and the relatively short necking stage. In corrosive media, they fail during the quasi-elastic loading stage at about $0.9\sigma_y$. The pre-strained specimens demonstrate slightly higher fracture stress and fracture strain than the as-received counterparts.

The alloy AZ31 specimens tested in air have the fully ductile dimpled appearance of the fracture surface as shown in Fig. 12.

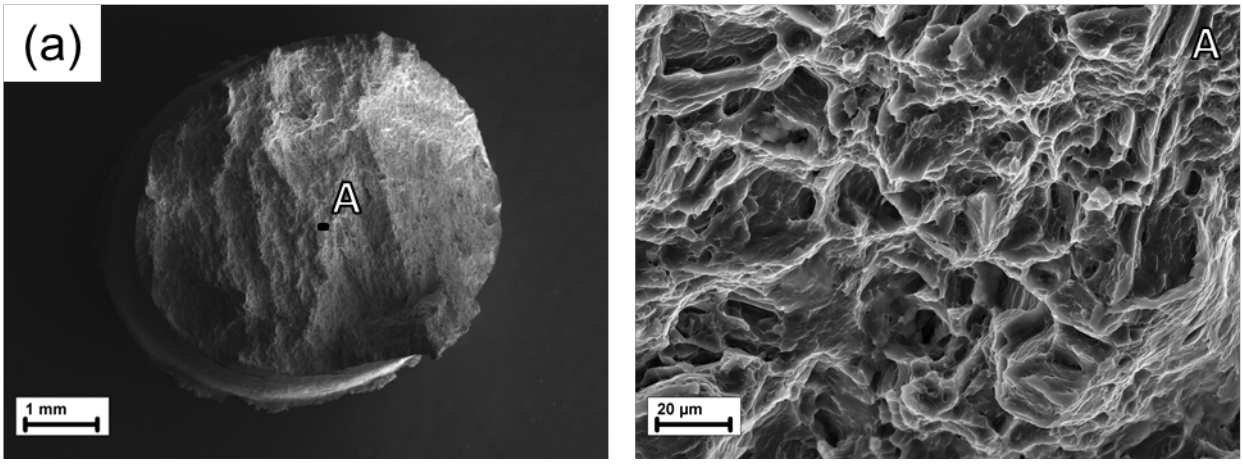

Fig. 12 – Fractographic SEM images of the AZ31 specimens tested in air: (a) – full view; (b) – the magnified region marked as A in (a) demonstrating the typical ductile dimpled relief.

The fracture surfaces of the AZ31 specimens SSRT tested in corrosive media demonstrate the larger fraction of the brittle relief and just a little amount of the ductile relief in comparison with the ZK60 samples, Fig. 13. No shear lips (such as those typically seen in the subzone 3-2 in ZK60) were observed. Apparently, the cracks originated at multiple sites on the side surface and propagated towards the centre just as in the case of ZK60. Almost the whole peripheral part of the fracture surface can be associated with the first brittle zone having the largely fluctuating length. This zone is composed of a mixture of intergranular and cleavage facets as illustrated in Figs. 13c-f. In conformity with the greater average grain size in the AZ31 specimens, both kinds of facets have larger dimensions if compared with those found in the first zone of the ZK60 specimens. The a_1 length in the AZ31 specimens varies from 800 to 1250 µm. This is as twice as large in comparison with the a_1 values in the alloy ZK60, c.f. Table 2. The greatest fraction of the fracture surface of the AZ31 specimens is covered by the fluted relief. Topological features of the fluted facets in the AZ31 specimens are similar to those in the ZK60 alloy, though the flutes are more pronounced and their diameter is larger, c.f. Fig. 14. The secondary cracks, such as those frequently found in the 2-2 zone in ZK60 specimens, are only occasionally found on the fracture surfaces of the AZ31 specimens. Some AZ31 specimens did not show them at all.

The effect of pre-straining on the fracture surface of AZ31 specimens is similar and even more pronounced in comparison to ZK60 specimens. After testing in corrosive media, the fracture surface of all AZ31 pre-strained specimens exhibits shear lips and large dimpled ductile area, Table 2. The total length of the zones a_1 and a_2 produced by SCC in the pre-strained specimens is about two times smaller than in their as-received counterparts. Lengths of both the first and the second brittle zones in the alloy AZ31 are reduced after pre-straining.

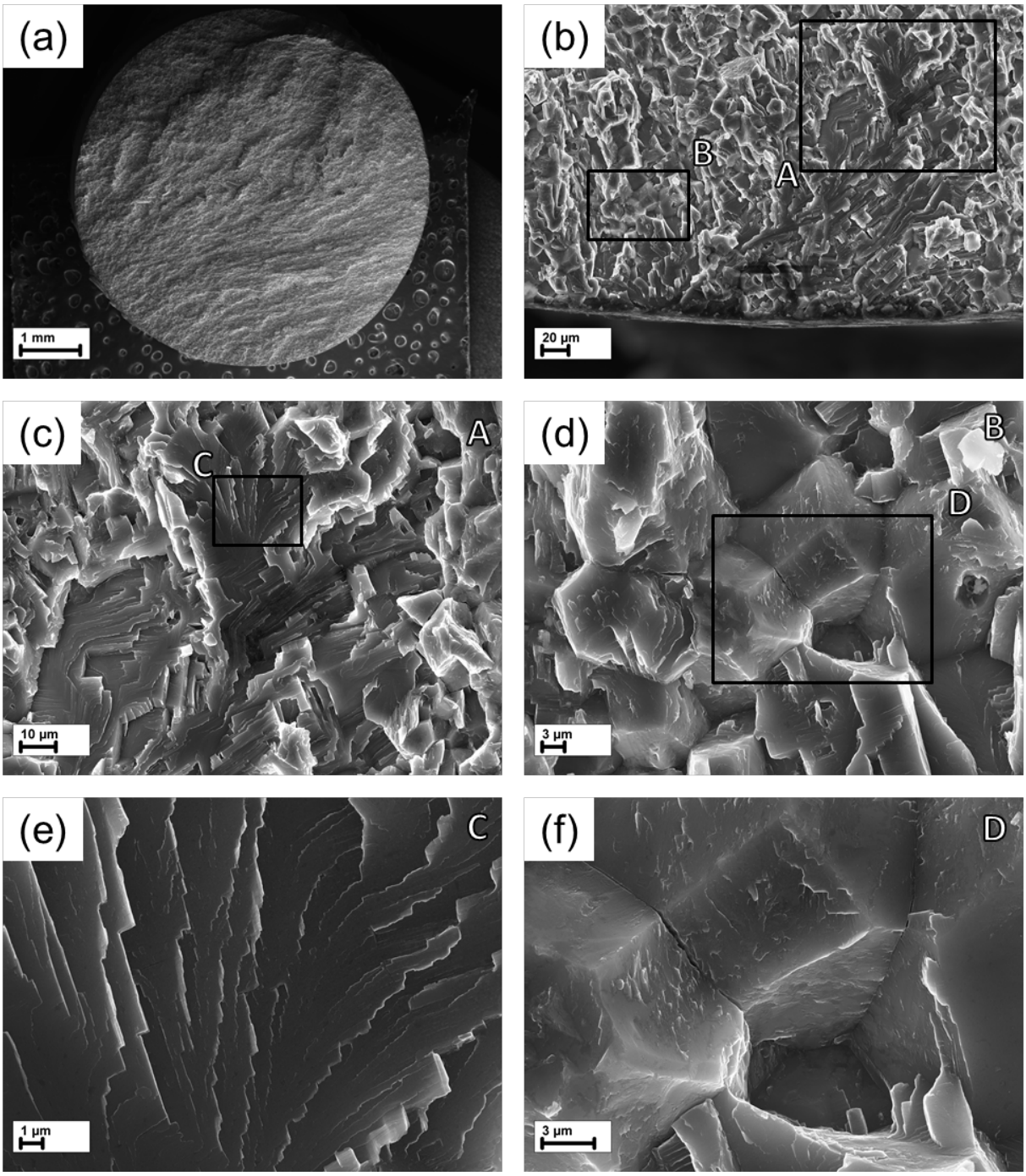

Fig. 13 – Fractographic SEM images of the AZ31 specimens tested in corrosive media: (a) – full view; (b) – general view of the zone a_1; (c) – the magnified region marked as A in (b) demonstrating cleavage facet surrounded by intergranular facets ; (d) – the magnified region marked as B in (b) with intergranular facets; (e) – the magnified region marked as C in (c) demonstrating interlocking river pattern of the cleavage facet; (f) – the magnified region marked as D in (e).

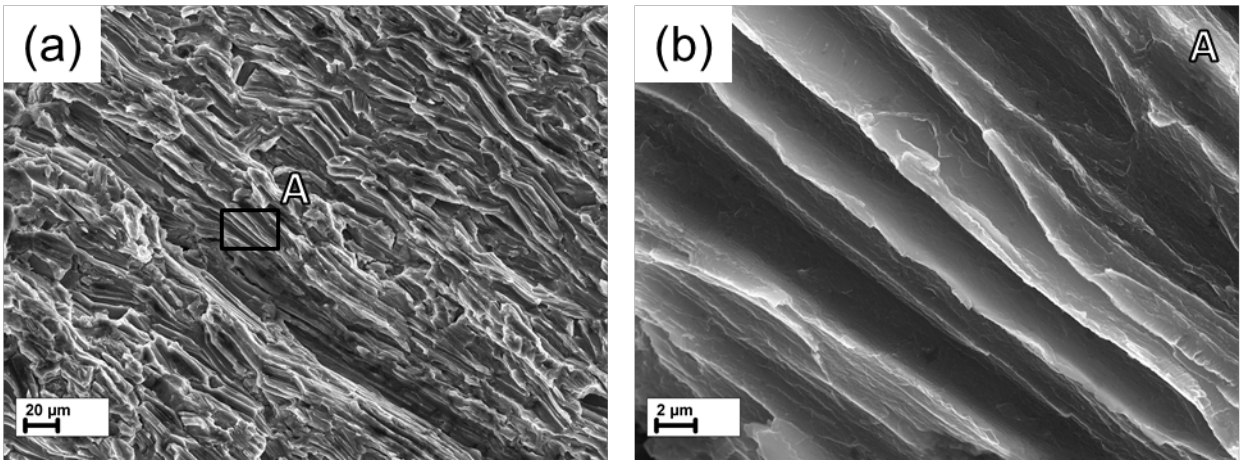

Fig. 14 – Fractographic SEM images of the zone a_2 featuring by fluted facets for the AZ31 specimens tested in corrosive media: (a) – the region with the dominated fluted morphology; (b) – the magnified region marked as A in (a) demonstrating typical flutes.

4. Discussion

4.1. The relationship between the fracture modes of SCC and mechanical properties

The results of the present study evidently show that the as-cast technically pure magnesium and its alloys tested in corrosive media exhibit distinct fractographic features specific for each material. On the other hand, at certain conditions which are described below, SCC occurs with the formation of the fluted morphology that is common to all investigated materials. The crack growth producing fluted facets is the primary fracture mode for as-cast Mg in corrosive media as well as in air, though the appearance of the flutes after SCC is somewhat different from those in air. The fracture of Mg during tensile testing in air and in the corrosive solution occurs by this mechanism from the beginning to the end of the test. As opposes to this, when both alloys were exposed to the corrosive environment, the fracture initiates at the surface and propagates inward through brittle intergranular and cleavage cracking. The SCC mechanism generating the fluted morphology comes into force only when the initial brittle crack reaches a “critical” length. Thus, it can be supposed that a certain value of the stress intensity factor K_f corresponding to a certain size of the plastic zone ahead of the crack tip is needed to activate the SCC mechanism producing fluted facets. Indeed, the analysis of the literature suggests that the formation of fluted facets can be associated with plastic deformation in the close-to-the-crack tip region. The fluted fracture surface markings are well-known fractographic feature of HCP metals and alloys such as titanium [19], zirconium [20,21] and magnesium [5,8] subjected to SCC and LME, albeit such fracture surfaces can be occasionally found in these materials even when the fracture occurred in

inert environment [8,19]. For example, during SCC or LME of titanium alloys, the fluted fracture surfaces usually interlink the cleavage cracks growing concurrently on parallel planes [19]. It was concluded that flutes, also termed "striations" or (slip) "river patterns", are ruptured halves of tubular voids which form on prismatic $\{10\bar{1}0\}$ planes by planar intersecting slip in the α-phase or at α-α and α-β interfaces [19]. They are primarily associated with near-basal cleavage, the role of which is to relax three-dimensional stresses and facilitate columnar slip on prismatic planes. Similar conclusions were drawn by Lynch and Trevena [8] who studied LME and SCC in pure Mg. They arrived at the conclusion that the "fluted fracture surfaces are produced probably because tubular voids are nucleated by the intersection of basal slip bands with prismatic or pyramidal slip bands. Voids are subsequently nucleated at second-phase particles or dislocation cell boundaries in highly strained regions between tubular voids producing more equiaxed dimples within flutes". As has been shown in the present study, the cracking process producing fluted morphology with the equiaxed dimples within the flutes is the common fracture mode in as-cast pure Mg tested in air. It was suggested elsewhere that fluted fracture is characteristic of materials in which the cross-slip is hindered [19]. It is therefore plausible to suppose that the formation of the fluted relief instead of the ordinary equiaxed large dimples is facilitated in pure Mg because of its strong propensity to planar (basal) slip and the limited number of possibly active non-basal slip systems at relatively low stresses and temperatures. Alloying is known as an effective means to reduce the critical resolved shear stress (CRSS) differences between different slip modes and affecting the twinning response during deformation. Therefore, after testing in air, the specimens of the AZ31 and ZK60 alloys demonstrate the fracture surfaces where the usual equiaxed large dimples prevail, although some poorly visible flutes are still found occasionally in the dimpled relief. *The main conclusion, which can be drawn from the above brief literature survey, is that the fluted morphology heralds a ductile (micro-void coalescence) fracture mode, and, as such, it's appearance must be preceded by considerable plastic deformation.* As-cast Mg has a very low yield stress in comparison with the alloys tested. Therefore, plastic deformation in this material commences almost immediately after the beginning of loading. This likely triggers the mechanism of SCC resulting in the formation of the fluted morphology at the very low stress when Mg specimens are tested in corrosive media. The present observations show that exposing the Mg specimen surface to the corrosive solution during tensile testing eliminates the small dimples within the flutes so that the surface of the latter becomes smoother than in air. This effect is exactly the same as that found by Lynch and Trevena [8]. They supposed that the adsorbed metal (in the case of LME) or hydrogen atoms (in the case of SCC) at crack tips facilitate the nucleation of dislocations from crack tips, and, thereby, promote the coalescence of cracks with voids ahead of cracks. Thus, both LME and

SCC occur through a more localised micro-void coalescence process than that in inert environments. The low yield stress and the strain-hardening behaviour of Mg specimens tested in corrosive media can be considered supportive of the adsorption-induced localised slip.

At early deformation stages, SCC of both alloys occurs by the mechanism producing the typically brittle intergranular and cleavage facets, which are obviously different from the fluted ones. The origin of such facets in Mg alloys failed due to SCC is often associated with HE caused by diffusible hydrogen [2,13] or by hydrides [2,7,9]. Nonetheless, it was suggested in [8] that these facets can also be formed by the adsorption-induced dislocation-emission (AIDE) mechanism. Recently it was found by some of the present authors [18], that the concentration of diffusible hydrogen in the specimens after SCC is negligible (notice that in the present study we used same alloys and specimens as those in [18]). Thus, it was supposed that the role of diffusible hydrogen in the SCC of Mg alloys is minor. One of the probable mechanisms of SCC responsible for the intergranular and cleavage facets is brittle cracking of Mg hydrides, which may form in the grains or along the boundaries. However, additional investigations are required to verify this hypothesis. It can be suggested that as the critical length of a cleavage/intergranular crack is reached, the plastic zone ahead of the crack becomes large enough to activate the mechanism producing fluted facets in the investigated Mg alloys. It should be noted that the fluted fracture is uncommon for these alloys when they are tested in air. This implies that the corrosive environment at the crack tip promotes the planar slip and/or restricts the cross slip. This is also supported by the disappearing equiaxed dimples within the flutes on the fracture surface of pure Mg tested in the corrosive solution.

4.2. Effect of pre-straining on the mechanism of crack growth

The intriguing result of the present study is that after pre-straining the Mg alloys tested in corrosive media demonstrate higher mechanical properties as well as more ductile fracture surface in comparison with their as-received counterparts. The explanation of such an effect can be related to the increased yield stress of these alloys which is caused by strain-hardening. Indeed, the correlation exists between the stress of onset of apparent plastic deformation and the SCC threshold stress σ_{scc}, was reported for many materials, including steels [22, 23], Cu- [24] and Mg-based alloys [25]. It is suggested that plastic deformation accompanied by dislocations slip emerging to the metal surface can be required to break the Mg hydroxide surface film protecting the juvenile metal surface from the contact with adsorbed hydrogen or other surface-active agents [26]. During tensile testing in the corrosive solution, plastic deformation in the specimens pre-strained in air should begin at the stress higher than in the as-received specimens.

Thus, if plastic deformation is a prerequisite for crack nucleation, which occurs at the SCC threshold stress σ_{scc} in the as-received specimens the pre-straining should increase this stress up to $\sigma_{scc}^{ps} > \sigma_{scc}$. It should be noted that the local yielding in most metals and alloys commences at stresses much lower than the macroscopic yield stress determined from the stress-strain diagram at the 0.2% offset strain. In particular, this is witnessed by the acoustic emission signal [27], which commonly arises in Mg alloys shortly after the beginning of loading. Thus, the values of σ_{scc} and σ_{scc}^{ps} are expected to be well below the macroscopic yield point, which is in excellent agreement with a large volume of experimental data revealing that σ_{scc} for various Mg alloys ranges commonly between 40-80% of the yield stress [25]. The pre-straining can result in an increase in crack initiation stress. However, to explain its effect on the fracture surface appearance and mechanical properties, the kinetics and the mechanism of SCC should be considered in some detail.

Using the DC potential drop technique Winzer et al. showed that, after initiation, the SCC in Mg alloys occurred at a gradually growing true stress until the final unstable fracture happened at certain critical stress [26]. Thus, the final mechanically unstable fracture was preceded by the subcritical environmentally-assisted crack growth that required both the increasing external stress and the presence of corrosive media at the crack tip. The brittle subcritical crack propagation during SCC in Mg alloys is generally believed to occur as a sequence of brittle crack jumps through the consistently forming local regions of environmentally-embrittled metal ahead of the crack tip. The discontinuous SCC producing brittle cleavage-like facets in Mg-Al alloy was witnessed by the acoustic emission technique in [10]. According to these generally accepted views, the subcritical crack growth at $a<a_1$ in the present study is discontinuous by nature and is controlled by the interaction of a bare metal at the crack tip with the corrosive solution. We suggest the following scenario, which self-consistently accounts for the observed experimental findings. Ones the crack is nucleated at the specimen's surface at σ_{scc} or σ_{scc}^{ps}, the crack surface becomes exposed to corrosive media. The interaction of aggressive environment with the juvenile crack surface induces embrittlement of the close-to-surface region of the metal ahead of the crack tip, regardless of minute details of the active embrittlement mechanism. At some critical external stress, the brittle mechanistic crack jump occurs through this embrittled region producing intergranular and cleavage facets. This jump is followed by the crack arrest and plastic blunting when the crack reaches the ductile metal which is unaffected by corrosive media yet. The time is needed for corrosive media to produce a new embrittled region. During this time, the external stress increases due to moving traverse of the testing machine. Thus, at the constant and sufficiently high imposed strain rate, the sub-critical

crack growth occurs at the overall increasing far-field stress just as it is reported in [28]. The intermittent crack stop-and-go cycles involving formation and cracking of the embrittled region followed by crack arresting and blunting repeat themselves again and again until the crack reaches the critical length a_1 corresponding to K_f at which the crack growth mechanism alters to the one producing fluted relief. Thereby, the mechanism of individual crack jumps during the subcritical crack growth at $a<a_1$ is purely mechanistic, albeit the conditions necessary for these jumps are furnished by the corrosive environment. The exact mechanism of the crack growth producing the fluted relief, as well as the external stress at which this mechanism comes into play is not known yet and is a subject of the forthcoming research. Nevertheless, since the corrosive environment at the crack tip is also needed for operation of this mechanism, the kinetics of the crack growth at $a_1<a<a_2$ is supposed to be similar to that at $a<a_1$, i.e. the cracking probably occurs discontinuously at the progressively increasing far-field true stress.

If the aforesaid is correct, the obtained in the present study results can be explained as follows. Let us assume that the zones 1 and 2 with the lengths a_1 and a_2, respectively, distinct on the fracture surfaces of the specimens of the ZK60 and AZ31 alloys were produced by the stable sub-critical crack growth process that initiated at the threshold stresses σ_{scc} and $\sigma_{scc}^{ps} > \sigma_{scc}$ in the as-received and pre-strained specimens, respectively. When the length of the main crack reaches its critical value $a_c = a_1+a_2$ with the corresponding stress intensity K_c, the ductile rupture occurs due to the unstable crack growth.

The dependence of the critical external stress σ_c on the crack length for this Kc at which the unstable crack starts to evolve can be illustrated schematically as shown in Fig. 15. If the cracks in the as-received and pre-strained specimens during the test in corrosive media propagate with nearly the same velocity $da/d\sigma$ at the gradually increasing far-field true stress σ, the dependence of the crack length a on σ can be represented by the ascending solid lines correspondingly labelled in Fig. 15. It should be noted that the exact dependence of the external stress σ vs crack length a is unknown and can be complex. For example, the crack growth velocities at a_1 and a_2 are likely different because different SCC mechanisms are expected to operate at these fracture stages. However, since the relatively sub-critical crack growth assumes the increasing far-field true stress during monotonic tension (regardless of the exact mechanism), the ascending function of the $\sigma(a)$ is plausibly anticipated as depicted by the linear (solely for simplicity of illustration) $\sigma(a)$ functions plotted in Fig. 15. Thus, the main conclusions drawn from the schematic Fig. 15 should not depend on the assumption of the linearity of these functions.

As can be seen from Fig. 15, the critical crack length a_c for the as-received specimens is larger and the critical stress σ_c corresponding to the onset of the unstable crack growth is lower

those that for the pre-strained ones. This is in full agreement with the results of the fractographic analysis, which shows that the lengths a_1 and a_2 are both greater for the as-received specimens than for the pre-strained ones, Table 2. It was suggested above that the certain value of the stress intensity factor K_f is needed to activate the mechanism of SCC producing fluted morphology. Apparently, this value should be lower than K_c. The curve for the anticipated σ-a dependence for given $K_f < K_c$ is also provided in Fig. 15. In harmony with the results of fractographic observations, it follows from Fig. 15 that both lengths a_1^{ps} and a_2^{ps} for the pre-strained specimens should be smaller than those in the as-received specimens.

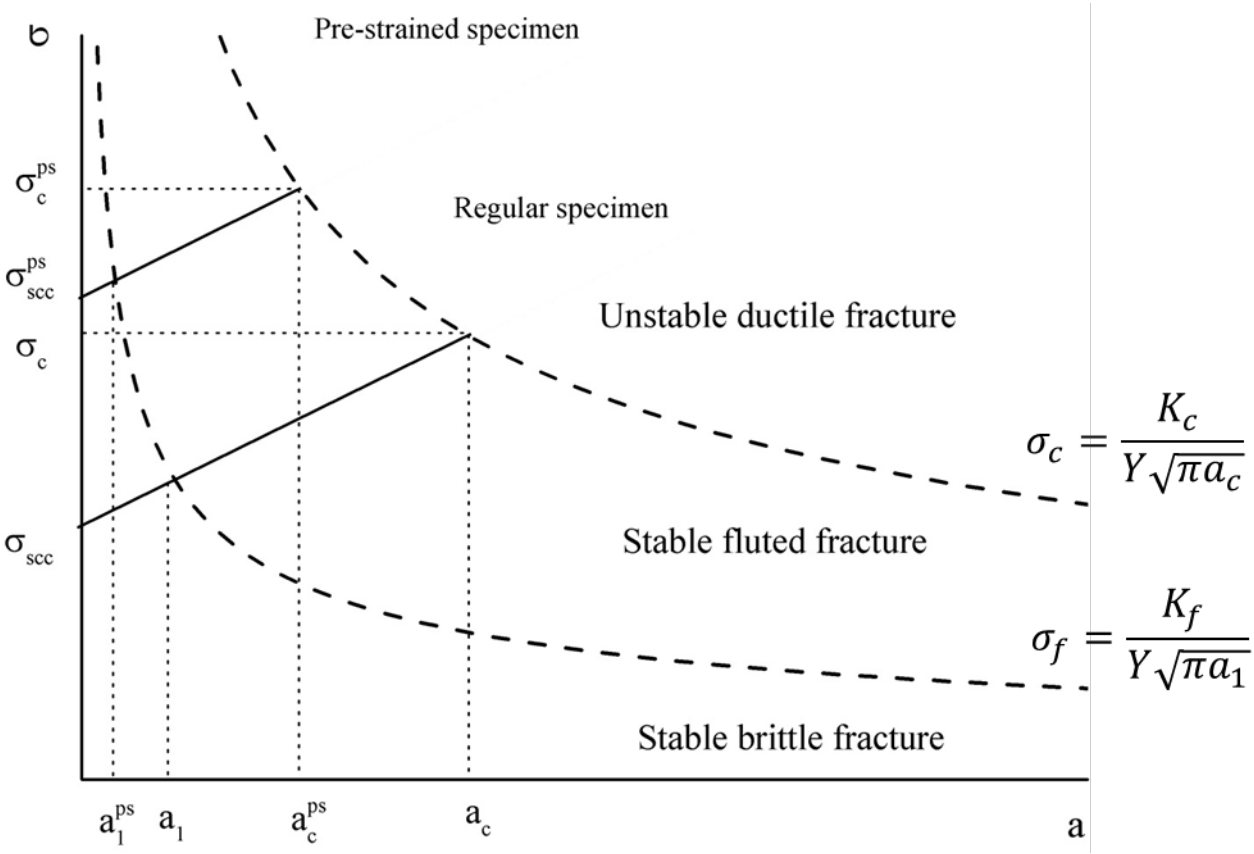

Fig. 15 – Schematics illustrating the stress vs crack length relationship for a given critical stress intensity factor K_c corresponding to the onset of the unstable crack growth and ductile fracture, and the same plot for the stress intensity factors K_f corresponding to initiation of the fluted relief due to the stable crack propagation in the corrosive solution (dashed lines); assuming that the SCC initiates at the threshold stress of σ_{scc} or σ_{scc}^{ps} and propagates with a constant velocity (solid lines) the transitions between different characteristic fracture zones (brittle→fluted→ductile) is expected at different crack lengths, depending on the amount of pre-strain.

According to the schematics shown in Fig. 15, the lengths of the specific SCC zones on a fracture surface of the Mg alloys specimens as well as the critical stress at rupture σ_c depend on

the following material-dependent variables: (i) the threshold stress σ_{scc} at which the crack initiates, (ii) the crack growth velocity $da/d\sigma$ and (iii) the stress intensity factors K_f and K_c. In particular, Fig. 15 predicts that at the very high crack growth velocity and low σ_{scc}, the fracture surface can be completely composed of cleavage and fluted facets without any ductile dimpled regions. This can explain the almost complete absence of the ductile fracture appearance in the as-received AZ31 alloy specimens tested in corrosive media. Presumably, the K_f value for as-cast pure Mg is very low due to its low yield stress, so that, according to the diagram shown in Fig. 15, the brittle fracture ceases to occur, and the fluted fracture mode prevails as is observed experimentally. Besides, it was shown above that the length of the brittle zone 1 is much larger for the AZ31 alloy than that for ZK60, although the former has the lower yield stress, and, therefore, the smaller size of zone 1 is heuristically expected from Fig. 15 for the alloy AZ31. Nevertheless, the exact values of σ_{scc}, $da/d\sigma$ and K_f for the studied alloys are unknown yet. In fact, it is obvious from Fig. 15 that at a certain combination of these variables the a_1 can be indeed larger for low yield stress alloys having lower K_f values.

Not only the proposed schematics explains why the pre-strain increases the susceptibility of Mg alloys to SCC, giving rise to increasing σ_c^{ps} value compared to σ_c of the as-received samples, but also it provides new insights that could help in the development of SCC-resistant Mg alloys from the mechanistic viewpoint.

5. Conclusions

1. Fracture surfaces of the alloys ZK60 and AZ31 failed due to SCC are featured by (i) the close-to-side surface region of typically brittle intergranular and cleavage facets gradually transformed into (ii) the region of transgranular fluted facets optionally followed by the regions of (iii) fluted facets with secondary cracks, (iv) flat dimpled rapture and (v) slant dimpled rapture. In contrast, the fracture surface of as-cast technically pure Mg after SCC is mostly represented by the mix of fluted transgranular facets and occasional intergranular or cleavage facets.

2. The preliminary plastic strain introduced in air increases both the elongation and the stress at fracture of both alloys SSRT tested in corrosive media. Besides, the positive effect of pre-straining is seen in the increased fraction of the ductile mode visible on the fracture surface. This beneficial impact of pre-straining on the susceptibility of Mg alloy to SCC can be explained by the increase in the yield stress, which must be overcome to trigger plastic deformation needed to break the surface protective film.

3. The mechanism of SCC in the AZ31 and ZK60 alloys changes at a certain critical crack length as is indicated by the alteration in the fracture surface morphology from the typical

brittle intergranular and cleavage facets to the transgranular fluted facets. On average, this critical crack length, which is characterised by the extent of the intergranular and cleavage facets region, in AZ31 specimens is as twice as large than in the alloy ZK60.

4. It can be plausibly supposed that the transgranular fluted morphology is produced by SCC controlled by the adsorption-induced dislocation emission mechanism, while the typical brittle inter-/trans-granular facets are most likely produced by delayed hydride cracking.

5. The fracture mode of Mg-based alloys subjected to SCC as well as mechanical properties of these materials can be likely explained and predicted if the values are known for the following variables: (i) the threshold stress σ_{scc} at which the brittle crack initiates, (ii) the crack growth velocity $da/d\sigma$ and (iii) the critical stress intensity factors K_f and K_c for the initiation of the stable fluted and unstable dimpled fracture, respectively. The experimental assessment of these quantities with aid from quantitative fractography is still a challenge. It requires a dedicated experimental design effort and is a subject of the ongoing investigations.

6. Acknowledgements

Financial support from the Russian Science Foundation through the grant-in-aid No. 18-19-00592 is gratefully appreciated.

References

[1] A. Atrens, W. Dietzel, P. Bala Srinivasan, N. Winzer, M. Bobby Kannan, Stress corrosion cracking (SCC) of magnesium alloys, in: Stress Corros. Crack., Elsevier, 2011: pp. 341–380. doi:10.1533/9780857093769.3.341.

[2] N. Winzer, A. Atrens, W. Dietzel, G. Song, K.U. Kainer, Fractography of stress corrosion cracking of Mg-Al alloys, Metall. Mater. Trans. A Phys. Metall. Mater. Sci. 39 A (2008) 1157–1173. doi:10.1007/s11661-008-9475-8.

[3] R.S. Stampella, R.P.M. Procter, V. Ashworth, Environmentally-induced cracking of magnesium, Corros. Sci. 24 (1984) 325–337. doi:10.1016/0010-938X(84)90017-9.

[4] M. Bobby Kannan, W. Dietzel, Pitting-induced hydrogen embrittlement of magnesium-aluminium alloy, Mater. Des. 42 (2012) 321–326. doi:10.1016/j.matdes.2012.06.007.

[5] D.B. Prabhu, S. Dhamotharan, G. Sathishkumar, P. Gopalakrishnan, K.R. Ravi, Stress corrosion cracking of biodegradable Mg-4Zn alloy in simulated body fluid at different strain rates – A fractographic investigation, Mater. Sci. Eng. A. 730 (2018) 223–231. doi:10.1016/j.msea.2018.06.002.

[6] M. Kappes, M. Iannuzzi, R.M. Carranza, Hydrogen Embrittlement of Magnesium and Magnesium Alloys: A Review, J. Electrochem. Soc. 160 (2013) C168–C178. doi:10.1149/2.023304jes.

[7] D.G. Chakrapani, E.N. Pugh, The transgranular SCC of a Mg-Al alloy: Crystallographic, fractographic and acoustic-emission studies, Metall. Trans. A. 6 (1975) 1155–1163. doi:10.1007/BF02658523.

[8] S.P. Lynch, P. Trevena, Stress corrosion cracking and liquid metal embrittlement in pure magnesium, Corrosion. 44 (1988) 113–124.

[9] D.G. Chakrapani, E.N. Pugh, On the Fractography of Transgranular Stress Corrosion Failures in a Mg-Al Alloy, Corrosion. 31 (1975) 247–252. doi:10.5006/0010-9312-31.7.247.

[10] D.G. Chakrapani, E.N. Pugh, Hydrogen embrittlement in a Mg-Al alloy, Metall. Trans. A. 7 (1976) 173–178. doi:10.1007/BF02644454.

[11] N. Winzer, A. Atrens, W. Dietzel, V.S. Raja, G. Song, K.U. Kainer, Characterisation of stress corrosion cracking (SCC) of Mg – Al alloys, Mater. Sci. Eng. A. 48 (2008) 339-351.

[12] L.F. Zhou, Z.Y. Liu, W. Wu, X.G. Li, C.W. Du, B. Jiang, Stress corrosion cracking behavior of ZK60 magnesium alloy under different conditions, Int. J. Hydrogen Energy. 42 (2017) 26162–26174. doi:10.1016/j.ijhydene.2017.08.161.

[13] F. Tuchscheerer, L. Krüger, Hydrogen-induced embrittlement of fine-grained twin-roll cast AZ31 in distilled water and NaCl solutions, J. Mater. Sci. 50 (2015) 5104–5113. doi:10.1007/s10853-015-9064-3.

[14] I.M. Robertson, P. Sofronis, A. Nagao, M.L. Martin, S. Wang, D.W. Gross, et al., Hydrogen Embrittlement Understood, Metall. Mater. Trans. A. 46 (2015) 2323–2341. doi:10.1007/s11661-015-2836-1.

[15] S.P. Lynch, Hydrogen embrittlement phenomena and mechanisms, Corros. Rev. 30 (2012) 63–133. doi:10.1515/corrrev-2012-0502.

[16] S.P. Lynch, Environmentally assisted cracking: Overview of evidence for an adsorption-induced localised-slip process, Acta Metall. 36 (1988) 2639–2661. doi:10.1016/0001-6160(88)90113-7.

[17] M.L. Martin, M. Dadfarnia, A. Nagao, S. Wang, P. Sofronis, Enumeration of the hydrogen-enhanced localized plasticity mechanism for hydrogen embrittlement in structural materials, Acta Mater. 165 (2019) 734–750. doi:10.1016/j.actamat.2018.12.014.

[18] E. Merson, P. Myagkikh, V. Poluyanov, D. Merson, A. Vinogradov, On the role of hydrogen in stress corrosion cracking of magnesium and its alloys: Gas-analysis study,

Mater. Sci. Eng. A. 748 (2019) 337–346. doi:10.1016/j.msea.2019.01.107.

[19] D.A. Meyn, E.J. Brooks, "Microstructural Origin of Flutes and Their Use in Distinguishing Striationless Fatigue Cleavage from Stress-Corrosion Crack- ing in Titanium Alloys, in: L.N. Gilbertson, R.D. Zipp (Eds.), Fractography Mater. Sci. ASTMSTP 733, American Society for Testing and Materials, 1981: pp. 5–31.

[20] B. Cox, Environmentally-induced cracking of zirconium alloys - A review, J. Nucl. Mater. 170 (1990) 1–23. doi:10.1016/0022-3115(90)90321-D.

[21] T. Motooka, K. Kiuchi, Corrosion fatigue growth of zirconium in boiling nitric acid, Corrosion. 58 (2002) 535–540. doi:10.5006/1.3277645.

[22] J. Wang, A. Atrens, Analysis of service stress corrosion cracking in a natural gas transmission pipeline, active or dormant?, Eng. Fail. Anal. 11 (2004) 3–18. doi:10.1016/j.engfailanal.2003.08.001..

[23] Z.F. Wang, A. Atrens, Initiation of stress corrosion cracking for pipeline steels in a carbonate-bicarbonate solution, Metall. Mater. Trans. A Phys. Metall. Mater. Sci. 27 (1996) 2686–2691. doi:10.1007/BF02652362.

[24] D. Wu, H.S. Ahluwalia, H. Cai, J.T. Evans, R.N. Parkins, Cyclic loading effects in the environment sensitive cracking of α-brass, Corros. Sci. 32 (1991) 769–794. doi:10.1016/0010-938X(91)90090-C.

[25] N. Winzer, A. Atrens, G. Song, E. Ghali, W. Dietzel, K.U. Kainer, et al., A critical review of the Stress Corrosion Cracking (SCC) of magnesium alloys, Adv. Eng. Mater. 7 (2005) 659–693. doi:10.1002/adem.200500071.

[26] N. Winzer, A. Atrens, W. Dietzel, V.S. Raja, G. Song, K.U. Kainer, Characterisation of stress corrosion cracking (SCC) of Mg – Al alloys, Mater. Sci. Eng. A. 48 (2008) 339-351.

[27] A. Vinogradov, D. Orlov, A. Danyuk, Y. Estrin, Effect of grain size on the mechanisms of plastic deformation in wrought Mg-Zn-Zr alloy revealed by acoustic emission measurements, Acta Mater. 61 (2013) 2044–2056. doi:10.1016/j.actamat.2012.12.024.